ADVANCED MATERIALS INTERFACES

www.advmatinterfaces.de

Electronic Structure and Band Alignment of $LaMnO_3/SrTiO_3$ Polar/Nonpolar Heterojunctions

Tiffany C. Kaspar, Peter V. Sushko, Steven R. Spurgeon, Mark E. Bowden, David J. Keavney, Ryan B. Comes, Sahar Saremi, Lane Martin, and Scott A. Chambers*

The behavior of polar $LaMnO_3$ (LMO) thin films deposited epitaxially on nonpolar $SrTiO_3$(001) (STO) is dictated by both the LMO/STO band alignment and the chemistry of the Mn cation. Using in situ X-ray photoelectron spectroscopy, the valence band offset (VBO) of LMO/STO heterojunctions is directly measured as a function of thickness, and found that the VBO is 2.5 eV for thicker (≥3 u.c.) films. No evidence of a built-in electric field in LMO films of any thickness is found. Measurements of the Mn valence by Mn *L*-edge X-ray absorption spectroscopy and by spatially resolved electron energy loss spectra in scanning transmission electron microscopy images reveal that Mn^{2+} is present at the LMO surface, but not at the LMO/STO interface. These results are corroborated by density functional theory simulations that confirm a VBO of ≈2.5 eV for both ideal and intermixed interfaces. A model is proposed for the behavior of polar/nonpolar LMO/STO heterojunctions in which the polar catastrophe is alleviated by the formation of oxygen vacancies at the LMO surface.

1. Introduction

The observation of a two-dimensional layer of high mobility electrons at the interface between the perovskite band insulators $LaAlO_3$ (LAO) and $SrTiO_3$ (STO) has been attributed to an electronic reconstruction that occurs to mitigate the so-called polar catastrophe, which arises from the deposition of polar, alternately charged $(LaO)^{1+}/(AlO_2)^{1-}$ layers (in the [001] growth direction) on nonpolar $(SrO)^0/(TiO_2)^0$.[1] Although the intrinsic nature of the effects observed at the LAO/STO interface continues to be a subject of debate,[2] the original report has led to an explosion of research exploring the fascinating physics that can occur at polar/nonpolar oxide interfaces. Like LAO, orthorhombic perovskite $LaMnO_3$ (LMO) consists of formally polar $(LaO)^{1+}/(MnO_2)^{1-}$ layers in the pseudocubic [001] growth direction. Unlike LAO, however, bulk LMO exhibits A-type antiferromagnetic ordering below a Néel transition temperature of ≈140 K.[3] High-spin $Mn^{3+}(t_{2g}^{3\uparrow}e_g^{1\uparrow})$ exhibits strong Jahn–Teller splitting; cooperative distortions of the oxygen octahedra and subsequent *C*-type orbital ordering below ≈780 K lifts the degeneracy of the e_g band, resulting in electron localization and causing LMO to be a p-type Mott–Hubbard insulator.[4–6] The orbital ordering of LMO is also influenced by magnetic superexchange.[4,7] In contrast to many other transition metal perovskites, bulk LMO can readily accommodate both oxygen deficiency (through the formation of oxygen vacancies and compensating Mn^{2+}) and oxygen excess (through the formation of an equal number of La and Mn cation vacancies).[8]

A large built-in electric field of 0.24 V $Å^{-1}$[9] is predicted to occur on the LAO side of LAO/STO heterojunctions for LAO thicknesses less than the critical thickness for electronic reconstruction. This electric field has never been observed in experiments designed to detect it,[2,10,11] although a weaker, residual electric field has been inferred in thicker, electronically

Dr. T. C. Kaspar, Dr. P. V. Sushko, Dr. S. A. Chambers
Physical and Computational Sciences Directorate
Pacific Northwest National Laboratory
Richland, WA 99354, USA
E-mail: tiffany.kaspar@pnnl.gov

Dr. S. R. Spurgeon
Energy and Environment Directorate
Pacific Northwest National Laboratory
Richland, WA 99354, USA

Dr. M. E. Bowden
Environmental Molecular Sciences Laboratory
Pacific Northwest National Laboratory
Richland, WA 99354, USA

The ORCID identification number(s) for the author(s) of this article can be found under https://doi.org/10.1002/admi.201801428.

Dr. D. J. Keavney
Advanced Photon Source
Argonne National Laboratory
Argonne, IL 60439, USA

Prof. R. B. Comes
Department of Physics
Auburn University
Auburn, AL 36849, USA

S. Saremi, Prof. L. W. Martin
Department of Materials Science and Engineering
University of California
Berkeley, CA 94720, USA

Prof. L. W. Martin
Materials Sciences Division
Lawrence Berkeley National Laboratory
Berkeley, CA 94720, USA

DOI: 10.1002/admi.201801428

reconstructed LAO films.[12] Because LAO is a wide bandgap insulator and Al^{3+} is a d^0 cation, there are few electronic, magnetic, or chemical degrees of freedom available for LAO to alleviate the electric field. The two primary mechanisms are (1) charge transfer from LAO to the STO side of the interface, resulting in a two-dimensional electron gas (2DEG),[1] or (2) cation diffusion across the LAO/STO interface.[2] Polar distortion of the LAO is a third mechanism that has been predicted to partially reduce the built-in electric field.[13]

By contrast, the additional electronic, magnetic (in some cases), and chemical degrees of freedom in other complex oxides compared to LAO can lead to alternative mechanisms to alleviate the polar catastrophe. One example is manifested as NiO precipitation in La_2NiMnO_6 films 1–5 nm from the STO interface[14] and at the $LaNiO_3$/STO interface.[15] The formation of an NiO secondary phase appears to be driven by the formation of oxygen vacancies; at these polar/nonpolar interfaces, oxygen vacancy formation is favorable to reduce the magnitude of the built-in electric field.[14] Another mechanism to alleviate the polar catastrophe is a charge redistribution mechanism in which the interfacial charge remains on the L*M*O (*M* = transition metal) side of the L*M*O/STO interface, reducing the valence charge of interfacial cations without forming a 2DEG. This charge redistribution has been observed in $LaCrO_3$/STO[16] and $LaFeO_3$/STO heterojunctions.[17]

In LMO, density functional theory (DFT) calculations by Chen et al.[18] predict a built-in electric field of 0.177 V $Å^{-1}$ below a critical thickness of ≈7.3 Å. The presence of this electric field has not yet been experimentally verified. Electron accumulation has been observed on the LMO side of the interface (detected as the presence of Mn^{2+}) in LMO films as thin as 2 unit cells[18] (u.c., 1 u.c. of unstrained LMO is ≈3.9 Å[5,19]), and attributed to the electronic reconstruction within the polar oxide; a critical thickness of <2 u.c. matches well with the predicted critical thickness of ≈7.3 Å.[18] Interfacial conductivity analogous to that seen in LAO/STO is not observed in these LMO/STO heterojunctions, confirming that the electron accumulation is confined to the LMO and localized on Mn cations. This behavior is comparable to that observed in $LaCrO_3$/STO.[16] Indeed, there is spectroscopic evidence for the presence of a fraction of Mn^{2+} near the STO interface for thick (well past the critical thickness) LMO and insulating $(La_{1-x}Sr_x)MnO_3$ ($x \leq 0.3$) epitaxial films.[20]

Electron-doped LMO that possesses a mixture of Mn^{2+} and Mn^{3+} is known to exhibit ferromagnetism through a double-exchange mechanism.[21] At a critical thickness of 5[3,18] or 6[5] u.c., antiferromagnetic LMO films on STO become ferromagnetic, which is also attributed to electron accumulation as the electronic reconstruction occurs. Recent DFT calculations by An et al.,[22] however, predict that compressive strain is the primary mechanism to induce ferromagnetism in thin LMO films on STO, although surface oxygen vacancies in the thinnest films suppress it. According to their simulation results, the built-in electric field plays a secondary role in both the electronic reconstruction and the magnetic ordering. This is due, in part, to polar structural distortions (shifts of Mn and Ti relative to the lattice) that were predicted to partially compensate the built-in electric field. In contrast to the work on LMO/STO, heterojunctions of LMO with LAO withdraw electrons from the LMO layer, eliminating Mn^{2+} and oxidizing some Mn^{3+} to Mn^{4+}, but are still found to be ferromagnetic through Mn^{3+}/Mn^{4+} double exchange.[23]

The bandgap of LMO is reported to be in the range of 0.5–1.3 eV,[5,6,24–27] much smaller than that of STO (3.25 eV). It has been hypothesized[5] that the difference in magnitude of the STO bandgap compared to that of LMO would lead to a Type I (straddled) LMO/STO band alignment, with a relatively small valence band offset (VBO, predicted to be ≈0.6 eV by Chen et al.[18]) and a corresponding conduction band alignment that places the LMO conduction band minimum (CBM) substantially lower in energy than that of STO. This band alignment would confine carriers originating from the electronic reconstruction to the LMO side of the interface. By contrast, Nakamura et al.[6] deduced from capacitance measurements and photocurrent action spectra of LMO/*n*-STO heterojunctions that the valence band of LMO resides more than 2 eV above that of *n*-STO, placing the CBM of LMO approximately equal in energy to that of *n*-STO. Consistent with this result, charge transfer from LMO to STO, which reduces Ti^{4+} to Ti^{3+}, has been both observed[28] and predicted.[29]

To reconcile these two very different sets of results, we have directly probed the Mn and Ti valence states, valence band alignment, and the prospect of a built-in electric field in epitaxial LMO/STO heterojunctions as a function of LMO thickness. The Mn cations exhibit mixed valence in the thinnest LMO films, but are present primarily as Mn^{3+} for thicker LMO layers. We find no evidence of a built-in electric field in even the thinnest LMO films (2 u.c.). Significantly, the measured VBO is much larger than that predicted previously,[18] placing the CBM of LMO near or above that of STO. DFT simulations reported in this work confirm this magnitude of VBO. In light of these results, we propose a model for the electronic structure of LMO/STO heterojunctions in which the polar catastrophe is alleviated by oxygen vacancies on the LMO surface. Within this model, interfacial electron accumulation does not occur to a significant extent, which has implications for the magnetic and electronic properties of this system.

2. Results

LMO films grow pseudomorphically on STO(001). After deposition of 30 nm, the LMO film is still strained to the substrate, as shown in the high-resolution X-ray diffraction (XRD) reciprocal space map in **Figure 1**a. Analysis of the composition by Rutherford backscattering spectrometry (RBS) (Figure S1, Supporting Information) confirms that the cation composition of the 30 nm film is stoichiometric within the error of the measurement.

High-resolution electron energy loss spectra in scanning transmission electron microscopy (STEM-EELS) maps of 4 u.c. LMO/STO reveal a well-ordered atomic structure at the LMO/STO interface (Figure 1b). Although the nominal LMO thickness of this film is 4 u.c., a faint 5th u.c. can be seen on the LMO surface. This partial layer is consistent with the somewhat rough surface morphology observed by reflection high-energy electron diffraction (RHEED) (Figure S2, Supporting Information). No polar structural distortions, such

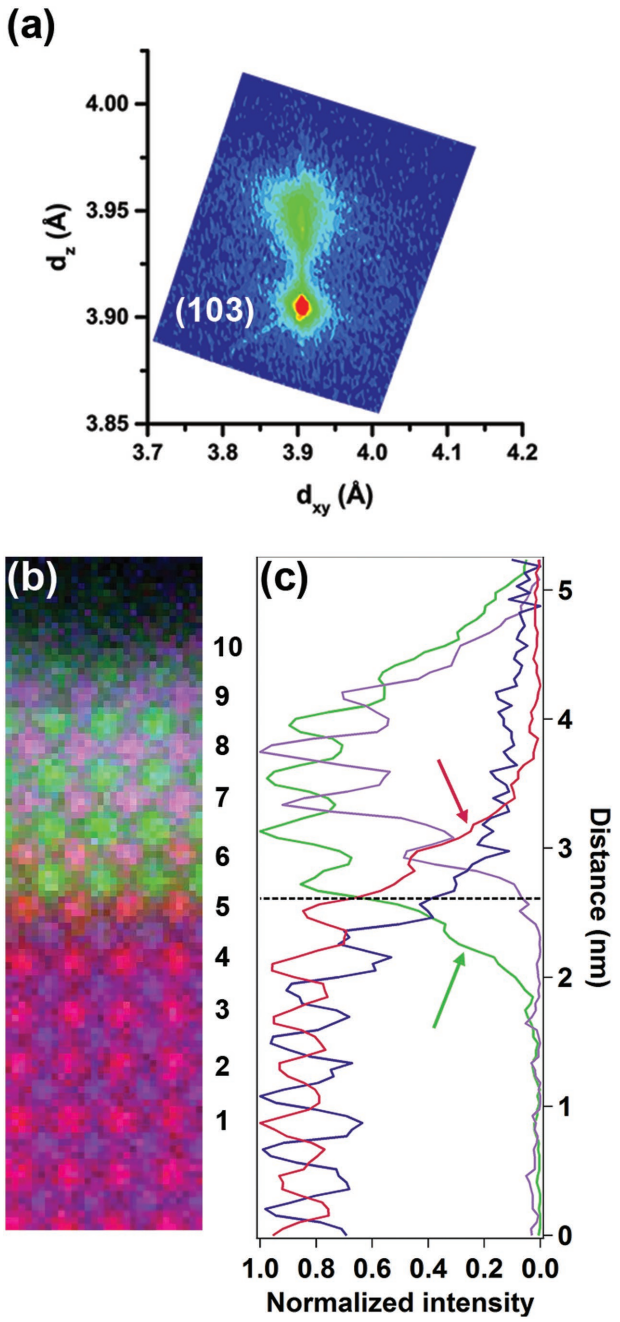

Figure 1. a) High-resolution XRD reciprocal space map of the LMO and STO (103) reflections of 30 nm LMO/STO(001), plotted as direct space map. b) High-resolution STEM-EELS composition map of 4 u.c. LMO/STO(001) measured along the STO[100] zone-axis. Green: La; purple: Mn; blue: Sr; red: Ti. c) EELS line profiles of La $M_{4,5}$ (green), Mn $L_{2,3}$ (purple), Sr $L_{2,3}$ (blue), and Ti $L_{2,3}$ (red) integrated signals. Signal intensities are normalized to their highest value. Arrows indicate diffusion of Ti (red) and La (green) across the interface.

as shifts of the Mn or Ti cations relative to the lattice, are observed. EELS line profiles (Figure 1c) reveal that Sr and Mn do not cross the interface to a significant extent, while in contrast, Ti (red trace) and La (green trace) both diffuse ≈1 u.c. across the interface.

2.1. Mn Valence

Figure 2 shows the Mn 2p, Ti $2p_{3/2}$, Sr 3d, and La 4d X-ray photoelectron spectroscopy (XPS) core-level spectra for heterojunctions of increasing LMO thickness. No changes in peak shape are observed for the Sr 3d or La 4d peaks as the LMO film thickness increases (Figure 2b), confirming that Sr and La are present exclusively as Sr^{2+} and La^{3+}, respectively, as expected. Comparison of the Ti $2p_{3/2}$ line shape in the LMO films to that of Ti in STO in Figure 2a confirms that Ti remains predominantly Ti^{4+} after deposition of LMO. However, weak intensity on the lower-BE side of the Ti $2p_{3/2}$ peak is observed, indicating the formation of a small amount of Ti^{3+} in the STO near the interface. This is illustrated by overlays of the Ti $2p_{3/2}$ peak from STO (dashed line) on the spectra for LMO films in Figure 2a, and is consistent with previous observations[28] and predictions[29] of charge transfer from LMO to STO. The intensity of this feature ranges from 0% to ≈5% of the total Ti $2p_{3/2}$ intensity, with a weak trend of increasing Ti^{3+} fraction as the LMO thickness increases.

Electron accumulation as a result of electronic reconstruction in thicker LMO layers would manifest as a reduction of some Mn^{3+} to Mn^{2+}.[18] However, since the Mn $2p_{3/2}$ BE shift between Mn^{2+} and Mn^{3+} is very small (≈0.3 eV),[30] it is difficult to assess the presence of Mn^{2+} from the relatively small shifts of the broad Mn $2p_{3/2}$ spectra in Figure 2a compared to the reference BE position (640.8 eV) of Mn $2p_{3/2}$ in a 30 nm thick LMO film. A general trend of decreasing Mn^{2+} and increasing Mn^{3+} concentration can be observed, however: the Mn $2p_{3/2}$ peak from 1 u.c. LMO is shifted to lower BE than the bulk reference, and exhibits some intensity around 645 eV; both the shift and the high BE intensity are indicative of the presence of Mn^{2+} and its associated satellite.[30–32] As the LMO thickness increases, the high BE satellite feature disappears and the primary Mn $2p_{3/2}$ peak shifts to slightly higher BE, indicating an increasing fraction of Mn^{3+}. The Mn $2p_{3/2}$ peak centroid does not shift fully to the position in thick LMO, however, which indicates that some Mn^{2+} is still present in the 4 and 6 u.c. LMO films. Although the BE shift between Mn^{2+} and Mn^{3+} is reported to be larger (>1 eV) for the Mn 3p core level,[32] a similar analysis of the Mn 3p spectra for the same LMO films does not reveal clear trends in Mn valence with increasing thickness, as shown in Figure S3 of the Supporting Information.

To determine the valence state of Mn in the thin LMO layers, Mn *L*-edge and O *K*-edge X-ray absorption spectroscopy (XAS) were employed. Although the chemical shifts in *L*-edge XAS (Mn 2p → Mn 3d) are similar in magnitude to those observed by Mn 2p XPS, changes in peak shape at the Mn *L*-edge between Mn^{2+}, Mn^{3+}, and Mn^{4+} are pronounced.[33,34] In particular, the strongest spectral feature from Mn^{2+} absorption occurs at ≈640 eV, while the strongest spectral feature from Mn^{3+} absorption occurs at ≈641.5 eV.[18,33,34] **Figure 3**a presents the Mn *L*-edge XAS for the same 2 and 4 u.c. LMO films (after transfer through air to the Advanced Photon Source) as measured in situ by XPS. The *L*-edge XAS line shape differs sharply between the two. The line shape for the 2 u.c. film indicates that Mn is present as a mixture of Mn^{2+} and Mn^{3+},[18,33,34] with Mn^{2+} as the predominant valence state. The 4 u.c. film, by contrast, contains primarily Mn^{3+}, although some Mn^{2+} is also present.

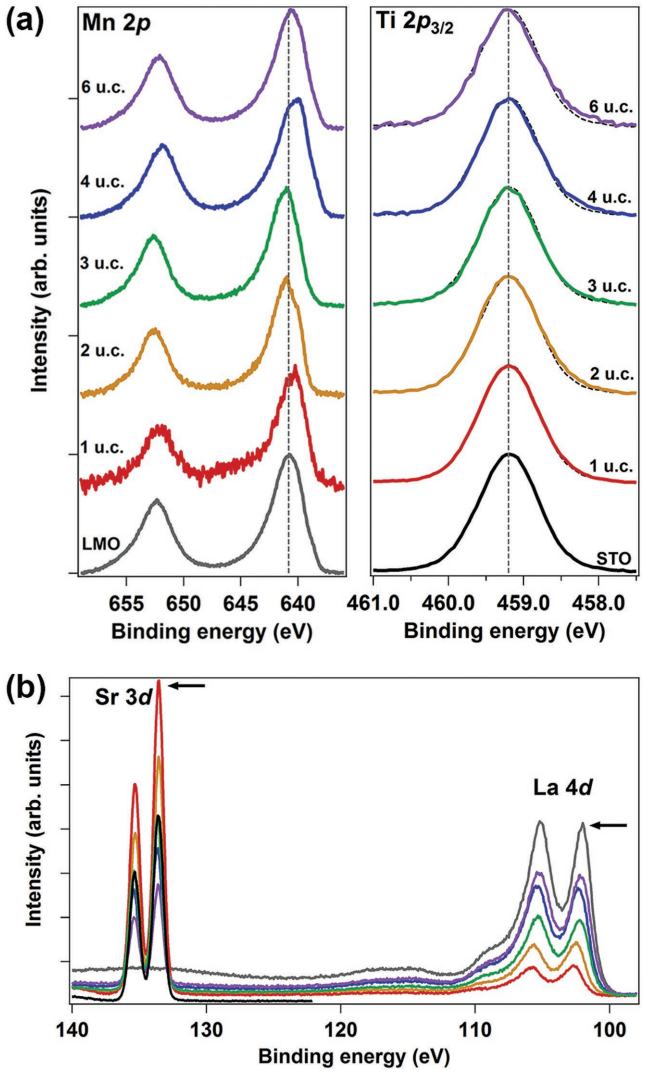

Figure 2. a) XPS core levels Mn 2p (left) and Ti $2p_{3/2}$ (right) for various thicknesses of LMO on STO. Mn $2p_{3/2}$ spectra have been aligned to place the lowest-BE La $4d_{5/2}$ peak at the value for 30 nm LMO, 100.5 eV, and Ti $2p_{3/2}$ spectra have been aligned at 459.2 eV. All spectra are normalized and vertically offset for clarity. A reference Mn 2p spectrum from the 30 nm LMO film (solid gray line) and a reference Ti $2p_{3/2}$ spectrum from a bare STO substrate (solid and dashed black lines) are presented for comparison. Vertical lines (640.8 eV, left, and 459.2 eV, right) are guides to the eye. b) XPS Sr 3d and La 4d core levels, collected in the same scan. The peaks used for band offset measurements are indicated by arrows. Spectra have been shifted to align the Ti $2p_{3/2}$ peak (as in part (a)); the LMO reference standard is shifted to visually align with the heterojunctions. Line colors in (b) correspond to those in (a).

The corresponding O *K*-edge data shown in Figure 3b possess significant signal from the STO substrate, precluding a quantitative analysis of the Mn valence state. The first O *K*-edge peak, located just above 530 eV, arises from transitions from O 1*s* to hybridized O 2p/Mn 3d states in LMO (and, analogously, O 1s → O 2p/Ti 3d states in STO). In Mn oxides, the position of this peak shifts to lower energy with increasing Mn oxidation.[34] The observed shift from the 2 u.c. LMO film to the 4 u.c. film is ≈0.1 eV to lower energy, which is consistent with the increased average Mn oxidation state observed in the Mn *L*-edge spectra (although the role of decreasing signal from the STO substrate with increasing LMO film thickness has not been assessed). The observed spectroscopic signature of Mn^{2+} for thinner LMO, and Mn^{3+} for thicker films, is qualitatively similar to the XAS results obtained by Chen et al.[18] XAS collected in total electron yield (TEY) is surface-sensitive, with a probe depth of ≈5 nm;[35] thus, the entire LMO film, including the interface, is probed in the measurement. Although there is a depth dependence of the TEY signal,[35] these spectra do not provide sufficient information to determine whether the Mn^{2+} signal originates from the LMO surface, the LMO/STO interface, or is distributed throughout the LMO film.

High-resolution STEM-EELS provides a measure of Mn valence state that is spatially resolved on the atomic scale (with a spatial resolution of ≈1–2 u.c.). Mn $L_{2,3}$-edge STEM-EELS spectra from 4 u.c. LMO/STO are presented in Figure 3c; the layer designations correspond to the STEM-EELS image in Figure 1b. The Mn L_3 peak in the film bulk (layers 7 and 8) appears at 641.7 eV, which is consistent with the Mn L_3 XAS peak position of 641.6 eV for Mn^{3+} in the same 4 u.c. film (Figure 3a). The Mn L_3 EELS signal from the first full Mn layer at the LMO/STO interface (layer 6) is not shifted to lower energy, which indicates that the Mn in this layer is also predominantly Mn^{3+}. By contrast, Mn at the film surface (layer 9 and partial layer 10) is shifted by ≈0.8 eV to lower energy, which indicates some reduction to Mn^{2+}. The apparent presence of Mn in layer 5 is due in part to the inherent spatial extent over which the EELS signal is collected (1–2 u.c.), as well as beam dechanneling effects as spectra are collected across the interface;[36] a small fraction of Mn diffusion across the interface has also likely occurred. The signal from this layer is weak, making it difficult to evaluate the precise peak position.

2.2. LMO/STO Band Alignments

XPS is a powerful technique to directly measure heterojunction band alignment[37] and the presence and magnitude of band bending and electric fields near a surface.[11,38] As shown in Figure 2b, the Sr 3d and La 4d core level peaks were collected in a single scan region from each LMO film to minimize differential charging effects. From these spectra, the VBO, $E_{VBO,HJ}$, for LMO/STO heterojunctions at each LMO thickness is calculated as

$$E_{VBO,HJ} = (E_{Sr3d} - E_{La4d})_{HJ} - \left[(E_{Sr3d} - E_{VBM})_{STO} - (E_{La4d} - E_{VBM})_{LMO}\right] \quad (1)$$

where the first term is the BE difference between the Sr $3d_{5/2}$ (E_{Sr3d}) and La $4d_{5/2}$ (E_{La4d}) peaks for the heterojunction (HJ) (black arrows in Figure 2b), the second term is the BE difference between the Sr $3d_{5/2}$ peak and the valence band maximum (VBM) for a bare STO substrate, and the third term is the BE difference between the La $4d_{5/2}$ peak and the VBM for the bulk-like 30 nm thick LMO film. The terms within the square brackets generate a fixed value that represents the expected separation between the Sr 3d and La 4d peaks in a heterojunction in which the valence band maxima of the two materials are aligned. Thus, as written in Equation (1), a positive value of $E_{VBO,HJ}$ indicates that the VBM of LMO lies higher in energy (closer to the Fermi level) than the

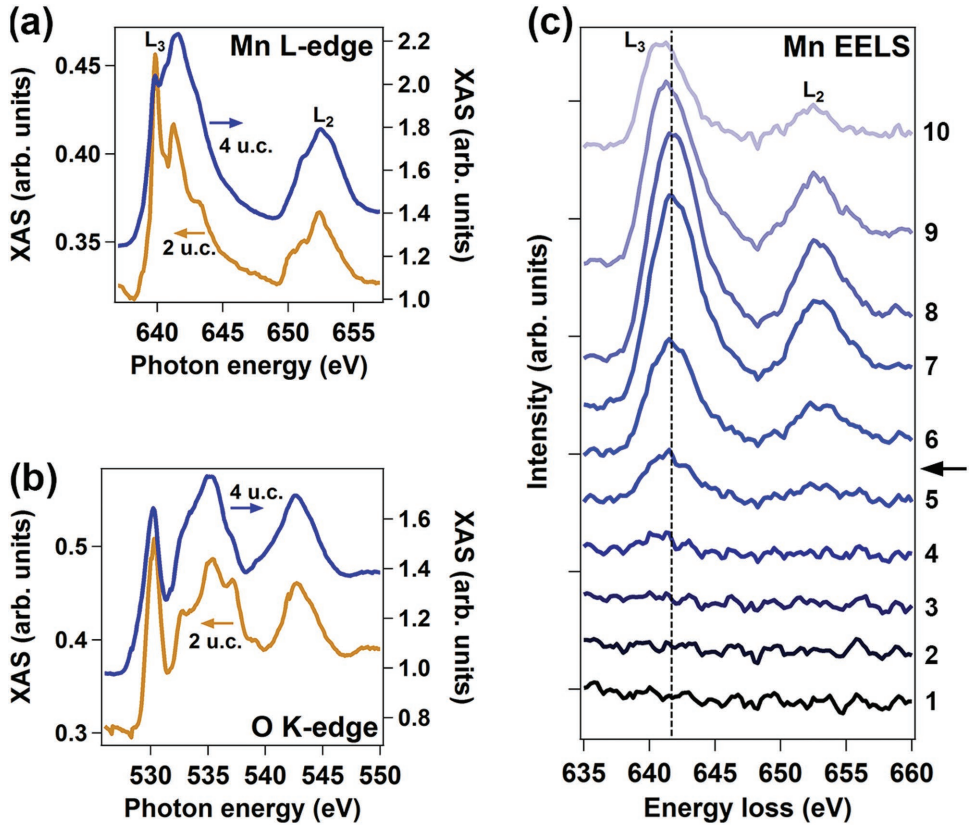

Figure 3. a) Mn *L*-edge XAS of 2 u.c. (left axis) and 4 u.c. (right axis) LMO on STO, collected in TEY mode. b) O *K*-edge XAS of 2 u.c. (left axis) and 4 u.c. (right axis) LMO on STO, collected in TEY mode. c) Layer-resolved Mn *L*-edge STEM-EELS spectra collected from 4 u.c. LMO on STO. Layer designations correspond to the STEM image in Figure 1b.

VBM of STO. As shown in Figure 4a, heterojunctions with 1 or 2 u.c. of LMO exhibit a VBO of ≈2.1 ± 0.1 eV. At 3 u.c. of LMO, the VBO increases to ≈2.6 ± 0.1 eV, and it remains ≈2.5 ± 0.1 eV for 4 and 6 u.c. films. This VBO is considerably larger than that assumed by Wang et al.[5] or that predicted by Chen et al.[18] A similar increase in VBO with increasing film thickness has been observed for $LaCrO_3$/STO[16] and $LaFeO_3$/STO[39] heterojunctions, with an increase from 1.9 to 2.55 eV (1.5 to 2.0–2.2 eV) as the $LaCrO_3$ ($LaFeO_3$) thickness increased.

The accuracy of the VBO calculated from Equation (1) can be confirmed for the measured heterojunctions by aligning the properly weighted VB spectra from the STO and LMO reference materials to reproduce the VBO calculated from Equation (1). In **Figure 4**b, this is done for the 4 u.c. LMO/STO heterojunction (which has been shifted to center the O 1s core level peak at 530.0 eV, a typical value for transition metal oxides). Summing the aligned and weighted reference VBs reproduces the overall shape of the heterojunction VB quite well, and both the leading edge (i.e., the VBM) and trailing edge align reasonably well with the experimental VB. From this, we conclude that a VBO of 2.5 eV appropriately characterizes the 4 u.c. LMO/STO heterojunction.

Because XPS only measures occupied states, it cannot provide information on the band structure above the Fermi level. Therefore, the conduction band offset (CBO) is typically calculated from the measured VBO using the bandgaps of each material in the heterojunction. For STO, the bandgap is well established as 3.2–3.3 eV;[40] here, we use 3.25 eV. By contrast, reported values for the optical bandgap of LMO range from 0.5–0.7 eV[26,27] to 1.0–1.3 eV.[5,6,24,25] This discrepancy arises primarily from two factors: (1) the bandgap of LMO is a function of oxygen content and shrinks with oxygen overstoichiometry,[25,27] and the oxygen content of the material likely varies significantly depending on the LMO preparation method; and (2) the different methods applied to determine the bandgap value from the optical absorption data, particularly in choice of region used for extrapolation of the leading edge of absorption.[6,24,26,27] Instead of photon absorption, Chainani et al.[25] used a combination of ultraviolet photoemission spectroscopy and bremsstrahlung isochromat spectroscopy (BIS, also known as inverse photoemission) to directly measure the bandgap of LMO, and determined the value to be 1.3 eV. For the 30 nm LMO film discussed here, the out-of-plane lattice parameter of 3.947 Å and the weak conductivity (measured by four-point probe at room temperature as ≈0.1 Ω^{-1} cm^{-1}) indicate that the film is nearly stoichiometric with respect to oxygen.[27] As indicated in Figure S4b of the Supporting Information, the fine structure of the absorption coefficient above the bandgap exhibits three peaks at ≈1.9, 2.3, and 2.6 eV, as expected for stoichiometric LMO.[41] The third peak at ≈2.6 eV is weak, and the spectroscopic ellipsometry (SE) data fits were not significantly degraded when excluding it. Extrapolation of the leading edge of the absorption spectrum results in a bandgap value of 0.79 eV (Figure S4b, Supporting Information). Assuming an indirect bandgap, a Tauc plot is constructed as $(\alpha h\nu)^{1/2}$ versus $h\nu$, with

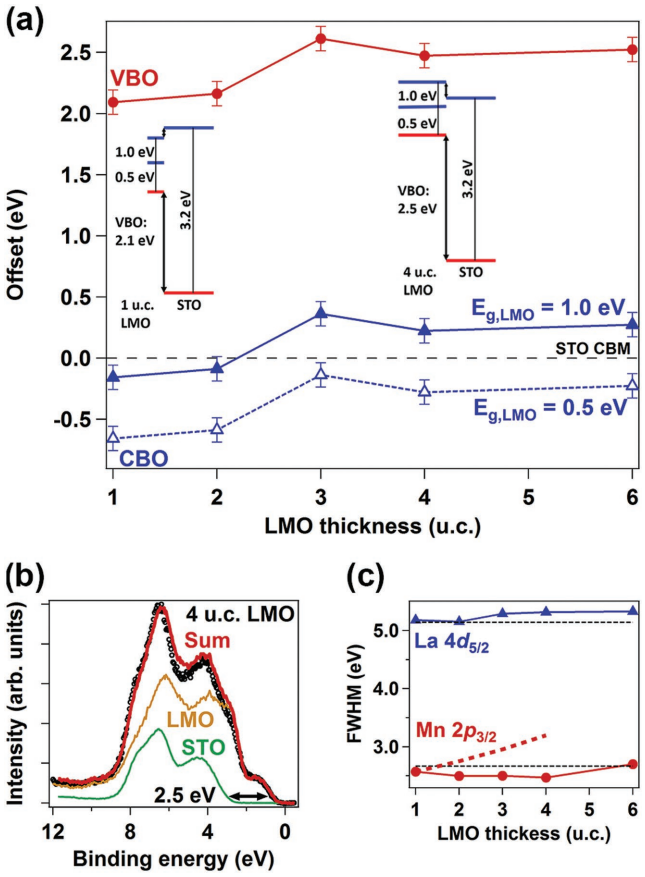

Figure 4. a) Valence band and conduction band offsets (VBO and CBO) for each LMO/STO heterojunction. CBO calculated for LMO bandgap (E_g) values of 0.5 (open symbols) and 1.0 eV (filled symbols). For both offsets, positive values indicate that the LMO edge is higher in energy than the STO edge. The CBM of STO is indicated with a black dashed line. Error bars (±0.1 eV) are estimated from error in determining core level peak positions. Insets: schematics of the band alignment for 1 u.c. (left) and 4 u.c. (right) LMO/STO heterojunctions. b) Valence band spectrum from 4 u.c. LMO/STO (symbols), along with shifted and attenuated spectra from a thick LMO film (yellow), a bare STO substrate (green), and their sum (red). c) FWHM of the Mn $2p_{3/2}$ and La $4d_{5/2}$ peaks from LMO for various thicknesses of LMO on STO. Horizontal dashed lines indicate the FWHM of the La $4d_{5/2}$ core level (top) and Mn $2p_{3/2}$ core level (bottom) from a thick LMO film. The dashed red line indicates the expected FWHM of the Mn $2p_{3/2}$ peak if the predicted built-in electric field of 0.69 eV u.c.$^{-1}$ were present.

the absorption coefficient $\alpha = 4\pi k/\lambda$; k is the extinction coefficient derived from modeling the SE data, λ is the wavelength of the incident light, and $h\nu$ is the incident photon energy. Linear extrapolation of the leading edge of this plot produces a bandgap value of 0.55 eV (Figure S4c, Supporting Information). These results are consistent with those of Smolin et al.,[26] and are representative of the bandgap of the thicker LMO heterojunction layers that contain primarily Mn^{3+} (i.e., 4 u.c. and thicker). The bandgap of very thin LMO layers possessing a large fraction of Mn^{2+} is unknown, but for the sake of analysis we assume that it is the same as for the thicker LMO layers.

While the LMO films studied here possess a bandgap of 0.55–0.8 eV, it is just as likely that the oxygen stoichiometry of other LMO films, deposited under somewhat different conditions, could possess a bandgap of ≈1.0 eV or greater. The difference between a bandgap of 0.55 eV and that of 1.0 eV could have a significant impact on the conduction band alignment with STO. In Figure 4a, two CBOs are plotted, assuming these two values for the bandgap (0.5 and 1.0 eV). The sign convention remains the same as for the VBOs: a positive CBO indicates that the CBM of LMO is higher in energy than the CBM of STO. For the LMO films measured here, possessing a bandgap of ≈0.5 eV, the CBM of LMO lies below that of STO, in agreement with the Type I band alignment hypothesized previously.[5,18] In this situation, free carriers arising from the electronic reconstruction will be confined to the LMO side of the interface. However, if LMO were to possess a bandgap of ≈0.7 eV or larger, the CBM of LMO would lie at or above the CBM of STO. With this Type II (staggered) band alignment, electron transfer from LMO to STO would occur.

2.3. Built-In Electric Field

Deposition of epitaxial, polar LMO on nonpolar STO(001) is expected to produce a built-in electric field in the LMO film that increases with increasing thickness until an electronic reconstruction occurs to remove it.[5] Built-in electric fields are manifested in XPS data as both a shift and asymmetric broadening of core level peaks originating in the film as a function of film thickness.[11,38] To evaluate whether a built-in electric field is present in our LMO/STO heterojunctions, the widths of the Sr 3d, Ti 2p, La 4d, and Mn 2p peaks were determined by fitting the spectra to Voigt functions and taking the full width at half maximum (FWHM) of the Voigt peak as the peak width (in the case of La 4d, the measured FWHM of the entire fitted envelope of peaks was taken as the peak width); the resulting peak widths are plotted in Figure 4c. The horizontal dashed lines represent the FWHM of the Mn 2p and La 4d peaks from the 30 nm thick LMO reference film. It is clear from Figure 4c that there is no systematic increase in peak width for either the La 4d or the Mn 2p peak. As a comparison, the Mn 2p spectrum from the 1 u.c. LMO film was attenuated, then shifted by the amount corresponding to the built-in electric field predicted previously[18] (0.177 V Å^{-1}, or equivalently 0.69 V u.c.$^{-1}$); these attenuated and shifted spectra were then summed to generate simulations of the Mn 2p peak from the 2, 3, and 4 u.c. LMO films with the built-in electric field present. The summed spectra were then fit with Voigt functions to extract the FWHM, and these values are plotted as a thick dashed line in Figure 4c. The significant increase in peak width predicted to occur due to the built-in electric field is not observed in the experimental data.

The lack of built-in electric field in LMO films of ≥2 u.c. thickness is consistent with the critical thickness of <2 u.c. observed by Chen et al.[18] However, the lack of Mn^{2+} at the LMO/STO interface in Figure 3c indicates that the mechanism of electronic reconstruction in this case is not simple charge transfer from surface Mn to interfacial Mn. To provide physical insight into the behavior of the LMO/STO system, we modeled the electronic structure of LMO/STO heterojunctions at the PBEsol and PBEsol+U levels of theory, accounting for the nonidealized interface structures. Supercells with abrupt and intermixed

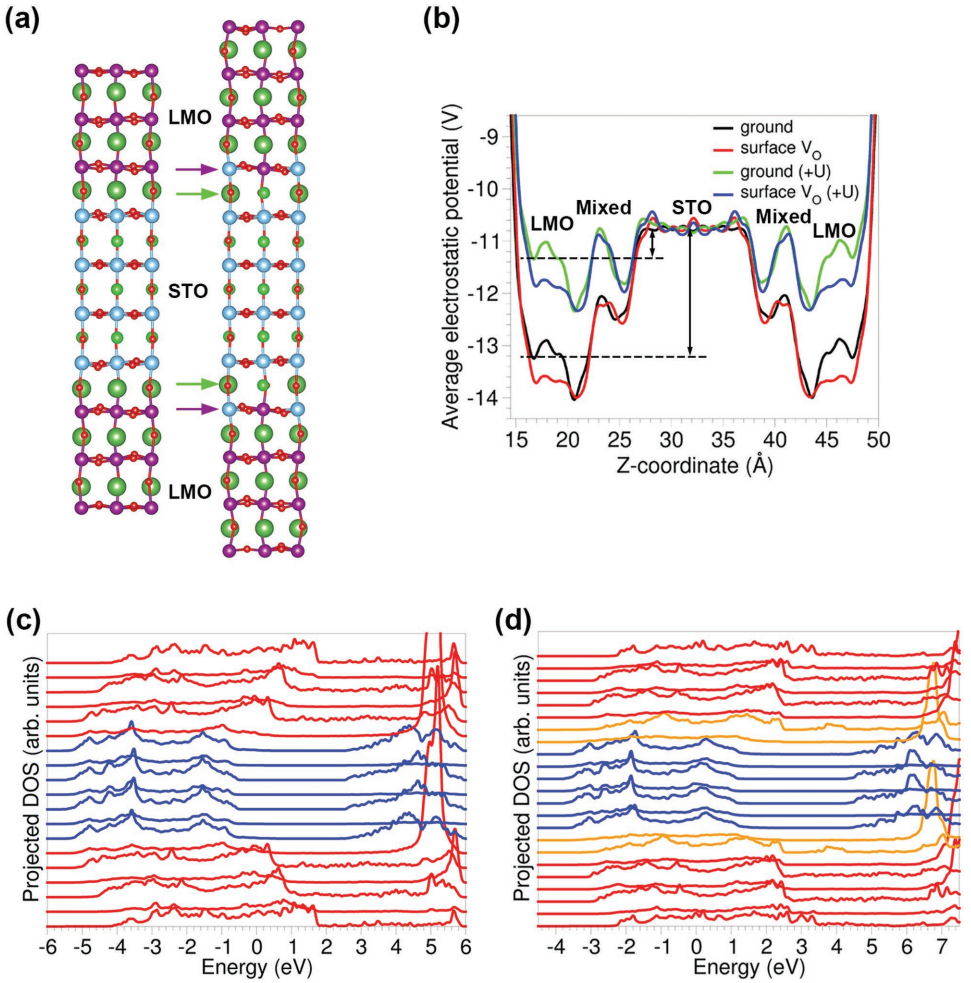

Figure 5. a) Supercells of idealized 3 u.c. LMO/3.5 u.c. STO/3 u.c. LMO (left) and intermixed 3 u.c. LMO/1 u.c. $(La_{0.5}Sr_{0.5})(Ti_{0.5}Mn_{0.5})O_3$/3.5 u.c. STO/1 u.c. $(La_{0.5}Sr_{0.5})(Ti_{0.5}Mn_{0.5})O_3$/3 u.c. LMO, relaxed with PBEsol. Purple: Mn; dark green: La; blue: Ti; light green: Sr; red: O. Purple arrows: $Ti_{0.5}Mn_{0.5}O_2$ layers; light green arrows: $La_{0.5}Sr_{0.5}O$ layers. b) Plots of potential versus depth of supercell for the intermixed cell shown in (a), with and without V_o, and with and without using the Hubbard *U* parameter in the single-point energy calculation. Dashed lines and arrows indicate the VBO between LMO and STO with or without the +U correction. The plots are shifted to place the potential in the STO layers at the same position for each calculation. c) Partial DOS plot for ideal 3 u.c. LMO/3.5 u.c. STO/3 u.c. LMO with abrupt interfaces and no V_o. STO layers are blue; LMO layers are red. d) Partial DOS plot for 3 u.c. LMO/1 u.c. $(La_{0.5}Sr_{0.5})(Ti_{0.5}Mn_{0.5})O_3$/3.5 u.c. STO/1 u.c. $(La_{0.5}Sr_{0.5})(Ti_{0.5}Mn_{0.5})O_3$/3 u.c. LMO with a single V_O at the LMO surface. STO layers are blue; $(La_{0.5}Sr_{0.5})(Ti_{0.5}Mn_{0.5})O_3$ layers are orange; LMO layers are red.

interfaces are shown schematically in **Figure 5**a. The intermixed interface was designed to resemble the single u.c. of La and Ti diffusion observed by STEM-EELS (see Figure 1). Including the Hubbard *U* parameter in the calculations was found to reproduce the experimental bandgap of STO ($E_{g,PBEsol+U}$ ≈3.3 eV) and increase the simulated VBO by ≈1.9 eV compared to the same calculation without including *U* (Figure 5b). The VBO can also be determined directly from the density of states (DOS) projected on each layer of the supercell, as presented in Figure 5c for the simulation of the abrupt interface. The VBO is determined by calculating the difference in VBM position between the TiO_2 layers in STO and the MnO_2 layers in LMO. However, the VBM position in the LMO layers increases as a function of distance from the STO interface, which is a manifestation of the built-in electric field. To best reproduce the XPS results, given that XPS is most sensitive to the topmost layer, it is appropriate to calculate the VBO as the difference between the STO layers and the outermost LMO layer. This method of VBO estimation is also in line with the analysis of Chen et al.,[18] who determined the VBO as the difference between the average potential in the STO layer and the average potential in the 6 u.c. thick LMO layer. For the 3 u.c. LMO simulation in Figure 5c, the VBO is 2.4 eV. As seen in Figure 5d, including cation intermixing and a surface oxygen vacancy in the simulation does not appreciably alter the resulting VBO. These VBO values match well with those measured experimentally (see Figure 4), but differ significantly from the VBO value of 0.6 eV predicted by Chen et al.[18] We note that optimizing the geometrical structure of the symmetric LMO/STO/LMO slab at the PBEsol+U level results in artificial elongation of the interatomic distances along the *c*-axis of the slab. For example, for U_{eff}(Ti) = 8.5 eV, the distance between the two outermost TiO_2 planes of the slab is 19.936 Å, which averages to 3.987 Å per unit cell or 2.1% larger than the experimental value of 3.905 Å. By contrast, if

Table 1. Built-in electric field in LMO layers calculated from the partial density of states for each configuration (see, for example, Figure 5c,d). For the intermixed interfaces with V_O at LMO surface, the surface layer is excluded. For the intermixed layers, the LMO thickness does not include the intermixed layer (one layer of $La_{0.5}Sr_{0.5}O$ and one layer of $Ti_{0.5}Mn_{0.5}O_2$) at the LMO/STO interface.

	Built-in electric field [eV u.c.$^{-1}$]		
LMO thickness [u.c.]	Abrupt interface	Intermixed interface	Intermixed interface, V_O at LMO surface
2	0.6	0.6	≈0
3	0.6	0.3	≈0

the relaxation is conducted at the PBEsol level, this distance becomes 19.417 Å, which averages to 3.883 Å per unit cell or ≈0.55% lower than the experimental value. A similar effect was found for the geometrical parameters in the LMO part of the slab. Furthermore, we found that the VBO calculated for such artificially distorted structures is only a few tens of an eV. Based on the magnitude of the lattice parameters and on the disagreement between the experimental VBO and the VBO calculated for the structures relaxed with PBEsol+U, we conclude that the U correction introduces significant error in the potential energy surfaces and its applicability for structure optimization should be carefully tested.

The built-in electric field predicted by the simulations is evident as a slope in the LMO potential in Figure 5b, and as a shift in the position of the partial DOS of each LMO layer as a function of distance from the STO interface in Figure 5c,d. The magnitude of this built-in electric field for both 2 and 3 u.c. (Figure 5c) LMO films with an abrupt interface is found to be ≈0.15 eV Å^{-1} (≈0.6 eV u.c.$^{-1}$, **Table 1**), which is nearly identical to the value predicted previously.[18] Interestingly, including 1 u.c. of interfacial intermixing in the simulation does not significantly alter the built-in electric field for 2 u.c. LMO, but the shift in partial DOS with thickness decreases somewhat as the LMO thickness is increased to 3 u.c. By contrast, including a single V_O at the LMO surface essentially eliminates shifts in the partial DOS in all but the surface layer for both 2 and 3 u.c. (Figure 5d) LMO, indicating that the magnitude of the electric field has been reduced to nearly zero. This reduction can also be seen qualitatively as a decrease in the slope of the potential in the LMO region in Figure 5b when a surface V_O is included in the simulation. Inclusion of V_O in the outermost MnO_2 layer results in a significant shift of this layer to higher energy compared to the deeper LMO layers. This shift is not a consequence of the polar/nonpolar interface, but instead is due to a combination of a surface shift (a smaller shift is observed at the surface of the 3 u.c. intermixed LMO layer without V_O) and the presence of the oxygen vacancy within the layer. As plotted in Figure S5a of the Supporting Information, as the LMO layer thickness increases, we find that the V_O formation energy decreases. This is consistent with previous results for other polar/nonpolar heterojunctions, such as La_2MnNiO_6/STO[14] and LAO/STO.[42] The presence of a surface V_O is shown in Figure S5b of the Supporting Information to redistribute electronic charge within the LMO layer, including reducing a neighboring surface Mn^{3+} to Mn^{2+}.[43]

3. Discussion

The Mn *L*-edge XAS spectra in Figure 3a indicate that the 2 u.c. LMO film possesses a higher fraction of Mn^{2+} than does the 4 u.c. film. These spectra are consistent with those measured by Chen et al.[18] for 3 and 5 u.c. LMO films deposited by pulsed laser deposition. *L*-edge XAS in TEY detection mode is a surface-sensitive technique,[35] and the decrease in Mn^{2+} signal as the LMO film thickness increases might be attributed to the effect of burying interfacial Mn^{2+} beneath stoichiometric (i.e., Mn^{3+}) LMO layers. However, the spatially resolved EELS spectra of 4 u.c. LMO (Figure 3c) reveal that Mn^{2+} is present at the LMO surface, not the interface. We reconcile these results by pointing out that the 2 u.c. film possesses much more Mn^{2+} than would be expected for either (a) an electronic reconstruction that transfers charge from surface Mn to interfacial Mn, or (b) the formation of surface oxygen vacancies and associated surface Mn^{2+}. Assuming an electron attenuation length of 20 Å and an exponential signal depth dependence analogous to that for XPS,[10] ≈55% of the total Mn L-edge XAS signal arises from the surface layer of 2 u.c. LMO and 45% arises from the interfacial layer. A low fraction of Mn^{2+} in either layer would produce an XAS spectrum with an overall low fraction of Mn^{2+}. Therefore, the high fraction of Mn^{2+} observed in the 2 u.c. film (on the order of 50% of the total Mn) must arise from a high fraction of Mn^{2+} in one or both layers. This high fraction of Mn^{2+} indicates that the 2 u.c. LMO film has not become fully oxygen-stoichiometric. This may be an intrinsic thickness effect, or a consequence of the short amount of time that the film was exposed to oxygen during the deposition. Either way, the properties of this oxygen-deficient film differ from those of thicker LMO films, as particularly evidenced by the decreased VBO exhibited by 1 and 2 u.c. LMO films on STO (see Figure 4a) compared to films of 3 u.c. and thicker. Taking the XAS and VBO results together, we conclude that, in this work, the intrinsic behavior of LMO films is only realized for films ≥3 u.c. thick. In these thicker films, Mn^{2+} is present on the LMO surface, not at the interface.

A Type I (straddled) band alignment with small VBO and large CBO was previously predicted for LMO/STO; such an electronic structure would strongly confine carriers to the LMO side of the interface.[5,18] By contrast, the band alignments measured for both ultrathin (1–2 u.c., predominantly Mn^{2+}, Type I alignment) and thicker (3–6 u.c., predominantly Mn^{3+}, Type II alignment) LMO indicate that electron transfer from LMO to STO may be facile, depending on the precise oxygen stoichiometry (and thus the bandgap) of the LMO layer. Even for LMO layers with a smaller bandgap (≈0.5 eV) and Type I band alignment, the CBO is <0.2 eV, which may serve to only weakly confine carriers to the LMO side of the interface. Indeed, Garcia-Barriocanal et al.[28] observed Ti^{3+} at the STO side of the LMO/STO interface that was hypothesized to arise from charge transfer from LMO, and thought to be responsible for interfacial magnetism in the heterojunctions. In this work, a weak indication of Ti^{3+} is observed in the XPS core level spectra in Figure 2a. The VBO measured here for thicker LMO films (2.5–2.6 eV) matches reasonably well with that reported by Nakamura et al.,[6] who experimentally measured a VBO of ≈2.2 eV and nearly equal CBMs for

an LMO/*n*-STO heterojunction. Likewise, the VBO of thicker $LaCrO_3$/STO heterojunctions was measured as 2.55 eV,[16] and the VBO of thicker $LaFeO_3$/STO heterojunctions was found to be 2.0–2.2 eV.[39] The partially filled d-bands of Cr^{3+} (d^3), Mn^{3+} (d^4), and Fe^{3+} (d^5) form occupied states at the top of the VB; these states are not present in STO because Ti^{4+} is a d^0 system. It has recently been hypothesized that band alignment at complex oxide interfaces is primarily determined not by the work functions or electron affinities of the constituent materials, but by continuity of oxygen valence states across the interface.[29] This continuity results in approximate energetic alignment of the O 2p-derived portions of the VBs of the two materials. If the O 2p-derived VBs of STO and LMO are aligned, the additional states at the top of the LMO VB that are derived from the partially filled d-states of Mn^{3+} will not be matched by any states at the top of the STO VB, and thus a fairly large VBO will result. From the VB simulation in Figure 4b, it appears that the main features in the VBs do align, producing a large VBO. This large VBO is confirmed by DFT calculations using PBEsol+U, which produce a VBO of 2.4 eV.

Predictions from DFT simulations for idealized LMO/STO in both previous[18] and current work are inconsistent with the experimental results that no built-in electric field is observed, even for the thinnest LMO layers. The cation intermixing considered in our model does not eliminate the built-in electric field, even though the spatial extent of intermixing and the corresponding concentration profile are comparable to what is observed experimentally. However, our simulations also show that the presence of V_O at the LMO surface can decrease the magnitude of the built-in electric field and simultaneously reduce surface Mn^{3+} to Mn^{2+}. Careful analysis of the atomic charge redistribution that occurs when a V_O is formed reveals that a surface Mn^{3+} is reduced to a valence close to, but not fully, Mn^{2+}, and the remaining charge is distributed in deeper layers and serves to reduce the magnitude of the built-in electric field. Although it is difficult to experimentally probe the presence of V_O directly, the presence of Mn^{2+} can be ascertained by spectroscopic methods. Indeed, we find Mn^{2+} at the LMO surface, but not the interface, in the 4 u.c. thick film (Figure 3c). This observation indicates that the predicted electronic reconstruction to eliminate the electric field (i.e., charge transfer from the LMO surface to the interface, resulting in surface Mn^{4+} and interfacial Mn^{2+}) has not occurred. In the absence of this reconstruction, the presence of Mn^{2+}, and the V_O that presumably gave rise to it, is somewhat unexpected given the highly oxidizing conditions in which the films were synthesized. However, our modeling shows that it becomes increasingly energetically favorable to form surface V_O as the LMO thickness increases, and we attribute the driving force for this behavior to the energetic gain as the magnitude of the built-in electric field is reduced. This driving force, likely aided by the ease with which Mn can alter its valence state from Mn^{3+} to Mn^{2+}, appears to be sufficient to accommodate V_O even under the highly oxidizing deposition conditions of oxygen-plasma-assisted molecular beam epitaxy (OPA-MBE). Thus, the built-in electric field, and subsequent electronic reconstruction, in LMO/STO heterojunctions is not observed experimentally because V_O formation results in charge redistribution that reduces or eliminates the electric field.

This model of V_O formation to compensate the built-in electric field has implications for both the ferromagnetism observed in LMO/STO heterojunctions and the possibility of forming a 2DEG at the LMO/STO interface. Ferromagnetism is only observed in LMO films once they have reached 5 or 6 u.c. thickness.[3,5,18] The lack of ferromagnetic ordering in thinner films may be due to the strong oxygen deficiency observed in this work in very thin LMO films, which appears to be difficult to avoid during deposition. Once a sufficient film thickness is reached, the film will achieve a nearly stoichiometric oxygen concentration, but oxygen vacancies and associated Mn^{2+} will still be present on the LMO surface. Double-exchange-mediated ferromagnetism can then occur in this surface region.

The conduction band alignment of LMO/STO heterojunctions is favorable (or nearly so) for electron transfer from LMO to STO, which raises the possibility of forming a 2DEG at the interface similar to that hypothesized for the LAO/STO system. This would require deposition or post-treatment of the LMO film to fill surface oxygen vacancies, allowing the electronic reconstruction to transfer charge to the LMO/STO interface; this charge could then be transferred to the STO side of the interface, forming a 2DEG. In this scenario, gated control of the 2DEG through manipulation of the oxygen stoichiometry can be envisioned.

4. Conclusions

The electronic structure and band alignment of polar/nonpolar LMO/STO heterojunctions have been explored both experimentally and theoretically. The heterojunction VBO is found to be large, 2.1–2.6 eV, in contrast to previous predictions[5,18] but in line with reported electronic transport measurements.[6] This large VBO places the conduction band of LMO near (<0.2 eV) or above the CBM of STO, indicating that under certain conditions (i.e., an oxygen stoichiometry that maximizes the bandgap of LMO), electron transfer from LMO to STO can be facile. No built-in electric field is observed by XPS core level peak analysis, even for films as thin as 2 u.c. From our DFT simulations, we attribute this lack of built-in electric field to the formation of V_O at the LMO surface. Surface V_O serve to reduce a neighboring Mn^{3+} to nearly Mn^{2+}, and the remaining charge is distributed in deeper LMO layers to counteract the potential gradient. Because the formation of V_O can decrease the magnitude of the built-in electric field, the V_O formation energy is predicted to decrease as the LMO thickness increases. Atomically resolved STEM-EELS maps of a 4 u.c. LMO/STO heterojunction confirmed the presence of Mn^{2+} on the LMO surface, corroborating the results of the DFT calculations. No Mn^{2+} was observed at the LMO/STO interface, confirming that the electronic reconstruction predicted to alleviate the polar catastrophe has not occurred.

5. Experimental Section

Film Synthesis: Epitaxial LMO films were deposited on STO(001) substrates by OPA-MBE. The STO(001) substrates were prepared with a TiO_2 termination by etching for 30 s in buffered HF, rinsing with

deionized water, then annealing in air at 1000 °C for 4 h. Annealed substrates were placed in a UV/O_3 cleaner for 5 min before being loaded into the vacuum system. Substrate surfaces were further cleaned in situ by exposure to activated oxygen from a differentially pumped electron cyclotron resonance (ECR) microwave plasma source at an oxygen pressure of 1.5×10^{-6} Torr and room temperature for 30 min to ensure removal of all residual carbon from the substrate surface. No C or F was detected on the STO surface in XPS survey scans after these treatment steps. The flow of activated oxygen continued as the substrate was heated to the deposition temperature of 650 °C. La and Mn were supplied from effusion cells to realize an LMO growth rate of 45 s u.c.$^{-1}$ (≈0.85 Å s^{-1}). Surface morphology and film thickness were monitored with RHEED patterns and intensity oscillations, respectively. After deposition, the heterojunctions were cooled in the flow of activated oxygen from the ECR plasma source.

Characterization: The heterojunctions were transferred through UHV to an appended chamber for in situ high-energy-resolution XPS measurements with monochromatic Al Kα X-rays and a VG/Scienta R3000 hemispherical analyzer. The energy resolution of the spectra presented here is better than 0.5 eV. A low-energy electron flood gun was utilized to compensate for charging effects during the measurements.

Ex situ high-resolution XRD patterns were collected on a Philips X'Pert materials research diffractometer using Cu Kα_1 radiation monochromated with a hybrid mirror/four-bounce monochromator. High-resolution θ–2θ scans were collected with fixed-slit detector optics. High-resolution reciprocal space maps were collected utilizing a three-bounce Ge analyzer crystal at the detector. Optical properties were measured with a J.A. Woollam variable angle spectroscopic ellipsometer (VASE) in the wavelength range of 0.4–5 eV (3100–248 nm). Data were fit with the WVASE software using Lorentz oscillators to model absorption and a Sellmeier model to simulate the real part of the optical response.

Cross-sectional STEM samples were prepared using an FEI Helios NanoLab DualBeam focused ion beam microscope and a standard lift out procedure along the STO [100] zone-axis, with initial cuts made at 30 kV/1° and final polishing at 2 kV/2.5° voltage/incidence angle. STEM-EELS data were collected on a JEOL ARM-200CF microscope operating at 200 kV, with a convergence semiangle of 27.5 mrad and collection angles of 42.9 mrad for fine structure measurements and 82.7 mrad for composition maps. Fine structure maps were collected using a ≈1 Å probe size with a ≈130 pA probe current and a 0.25 eV ch^{-1} dispersion, yielding an effective energy resolution of 0.75 eV. Composition maps were acquired with a 1 eV ch^{-1} dispersion and 4× energy binning to improve signal-to-noise. No plural scattering correction was performed, since zero loss measurements confirm that the samples are sufficiently thin ($t/\lambda < 0.5$ inelastic mean free paths).

Mn *L*-edge and O *K*-edge XAS were collected on beamline 4-ID-C at the Advanced Photon Source, Argonne National Laboratory using a helical undulator and a spherical grating monochromator. Samples were mounted with a beam incidence angle of ≈20°, and the absorption was measured at room temperature in TEY mode by monitoring the photocurrent. The monochromator was set for a bandwidth of 0.05%. The TEY data were normalized to the incidence flux monitored using a gold mesh upstream of the sample.

The film stoichiometry was probed via RBS within the Ion Beam Analysis Laboratory at Lawrence Berkeley National Laboratory. Studies were completed with a He^{2+}-ion beam energy of 3040 keV, an incident angle $\alpha = 22.5°$, an exit angle $\beta = 25.35°$, and a scattering angle $\theta = 168°$. Fits to the experimental data were completed using the analysis software SIMNRA (simnra.com).

Computational Methods: Computational models of the LMO/STO heterojunctions were generated using the periodic symmetric slab model (LMO/STO/LMO). The $\sqrt{2}a \times \sqrt{2}a$ lateral cell was used (a is the lattice parameter of STO, which was fixed at the experimental value of 3.905 Å) and out-of-plane c-parameter was set at 64 Å so that the vacuum gap is at least 20 Å wide. Relative energies of the heterojunction configurations and the corresponding one-electron densities of states were calculated using the Vienna ab initio simulation package.[44] The projector-augmented wave was used to approximate the electron-ion potential.[45] The PBEsol density functional[46] was used to find optimal slab geometrical structures, followed by a single point calculation of the electronic structure using PBEsol together with a rotationally invariant Hubbard $U_{eff} = U–J$ correction applied to Ti 3d states.[47] It is found that this procedure avoids artificial distortions of the lattice induced by the U correction. Heterojunction supercells were generated as 3.5 u.c. STO interfaced on both surfaces with 1, 2, or 3 u.c. of LMO. To account for interfacial intermixing, the configuration ...TiO_2/$(La_{0.5}Sr_{0.5})O$/$(Ti_{0.5}Mn_{0.5})O_2$ /LaO..., was considered, which has a cation concentration profile close to those observed experimentally. The $4 \times 4 \times 1$ Monkhorst–Pack grid was used for optimization of the structure and total energy calculations, while the $8 \times 8 \times 1$ grid was used for the calculations of the density of states. The plane-wave basis set cutoff was set at 500 eV. The Hubbard parameters U_{eff}(Ti) = 8.5 eV and U_{eff}(Mn) = 3.5 eV were used; these values of the Hubbard parameter were chosen because they reproduce the experimental bandgap of STO and are in line with values used previously.[18] The charge- and spin-density distributions were analyzed using the Bader method.[48] The energies of self-consistent calculations were converged to 10^{-5} eV per cell.

Supporting Information

Supporting Information is available from the Wiley Online Library or from the author.

Acknowledgements

T.C.K., P.V.S., S.R.S., M.E.B., and S.A.C. were supported by the U.S. Department of Energy (DOE), Basic Energy Sciences (BES), Division of Materials Sciences and Engineering, under Award No. 10122. R.B.C. acknowledges support from the National Science Foundation (NSF) under Grant No. DMR-1809847. S.S. acknowledges support from the U.S. DOE, BES, Division of Materials Sciences and Engineering, under Award No. DE-SC-0012375 for the study of complex-oxide materials. L.W.M. acknowledges support from NSF under Grant No. DMR-1608938. A portion of this research was performed using EMSL, a National Scientific User Facility sponsored by the U.S. DOE's Office of Biological and Environmental Research and located at Pacific Northwest National Laboratory. This research also used resources of the Advanced Photon Source, a U.S. DOE Office of Science User Facility operated for the DOE Office of Science by Argonne National Laboratory under Contract No. DE-AC02-06CH11357.

Conflict of Interest

The authors declare no conflict of interest.

Keywords

built-in electric field, $LaMnO_3$, oxygen vacancies, polar/nonpolar heterojunctions

Received: September 14, 2018
Revised: October 17, 2018
Published online:

[1] A. Ohtomo, H. Y. Hwang, *Nature* **2004**, *427*, 423.
[2] S. A. Chambers, *Surf. Sci.* **2011**, *605*, 1133.

[3] Y. Anahory, L. Embon, C. J. Li, S. Banerjee, A. Meltzer, H. R. Naren, A. Yakovenko, J. Cuppens, Y. Myasoedov, M. L. Rappaport, M. E. Huber, K. Michaeli, T. Venkatesan, Ariando, E. Zeldov, *Nat. Commun.* **2016**, *7*, 12566.
[4] N. N. Kovaleva, A. M. Oles, A. M. Balbashov, A. Maljuk, D. N. Argyriou, G. Khaliullin, B. Keimer, *Phys. Rev. B* **2010**, *81*, 235130.
[5] X. R. Wang, C. J. Li, W. M. Lu, T. R. Paudel, D. P. Leusink, M. Hoek, N. Poccia, A. Vailionis, T. Venkatesan, J. M. D. Coey, E. Y. Tsymbal, Ariando, H. Hilgenkamp, *Science* **2015**, *349*, 716.
[6] M. Nakamura, A. Sawa, J. Fujioka, M. Kawasaki, Y. Tokura, *Phys. Rev. B* **2010**, *82*, 201101.
[7] P. Ravindran, A. Kjekshus, H. Fjellvag, A. Delin, O. Eriksson, *Phys. Rev. B* **2002**, *65*, 064445.
[8] A. N. Grundy, M. Chen, B. Hallstedt, L. J. Gauckler, *J. Phase Equilib. Diffus.* **2005**, *26*, 131.
[9] J. Lee, A. A. Demkov, *Phys. Rev. B* **2008**, *78*, 193104.
[10] S. A. Chambers, M. H. Engelhard, V. Shutthanandan, Z. Zhu, T. C. Droubay, L. Qiao, P. V. Sushko, T. Feng, H. D. Lee, T. Gustafsson, E. Garfunkel, A. B. Shah, J. M. Zuo, Q. M. Ramasse, *Surf. Sci. Rep.* **2010**, *65*, 317.
[11] Y. Segal, J. H. Ngai, J. W. Reiner, F. J. Walker, C. H. Ahn, *Phys. Rev. B* **2009**, *80*, 241107.
[12] G. Singh-Bhalla, C. Bell, J. Ravichandran, W. Siemons, Y. Hikita, S. Salahuddin, A. F. Hebard, H. Y. Hwang, R. Ramesh, *Nat. Phys.* **2011**, *7*, 80.
[13] R. Pentcheva, W. E. Pickett, *Phys. Rev. Lett.* **2009**, *102*, 107602.
[14] S. R. Spurgeon, P. V. Sushko, A. Devaraj, Y. G. Du, T. Droubay, S. A. Chambers, *Phys. Rev. B* **2018**, *97*, 134110.
[15] E. Detemple, Q. M. Ramasse, W. Sigle, G. Cristiani, H. U. Habermeier, E. Benckiser, A. V. Boris, A. Frano, P. Wochner, M. Wu, B. Keimer, P. A. van Aken, *Appl. Phys. Lett.* **2011**, *99*, 211903.
[16] S. A. Chambers, L. Qiao, T. C. Droubay, T. C. Kaspar, B. W. Arey, P. V. Sushko, *Phys. Rev. Lett.* **2011**, *107*, 206802.
[17] S. R. Spurgeon, P. V. Sushko, S. A. Chambers, R. B. Comes, *Phys. Rev. Mater.* **2017**, *1*, 063401.
[18] Z. H. Chen, Z. H. Chen, Z. Q. Liu, M. E. Holtz, C. J. Li, X. R. Wang, W. M. Lu, M. Motapothula, L. S. Fan, J. A. Turcaud, L. R. Dedon, C. Frederick, R. J. Xu, R. Gao, A. T. N'Diaye, E. Arenholz, J. A. Mundy, T. Venkatesan, D. A. Muller, L. W. Wang, J. Liu, L. W. Martin, *Phys. Rev. Lett.* **2017**, *119*, 156801.
[19] J. Rodriguez-Carvajal, M. Hennion, F. Moussa, A. H. Moudden, L. Pinsard, A. Revcolevschi, *Phys. Rev. B* **1998**, *57*, R3189.
[20] J. A. Mundy, Y. Hikita, T. Hidaka, T. Yajima, T. Higuchi, H. Y. Hwang, D. A. Muller, L. F. Kourkoutis, *Nat. Commun.* **2014**, *5*, 3464.
[21] P. Raychaudhuri, C. Mitra, P. D. A. Mann, S. Wirth, *J. Appl. Phys.* **2003**, *93*, 8328.
[22] M. An, Y. K. Weng, H. M. Zhang, J. J. Zhang, Y. Zhang, S. Dong, *Phys. Rev. B* **2017**, *96*, 235112.
[23] L. Wu, C. J. Li, M. F. Chen, Y. J. Zhang, K. Han, S. W. Zeng, X. Liu, J. Ma, C. Liu, J. H. Chen, J. X. Zhang, Ariando, T. V. Venkatesan, S. J. Pennycook, J. M. D. Coey, L. Shen, J. Ma, X. R. Wang, C. W. Nan, *ACS Appl. Mater. Interfaces* **2017**, *9*, 44931.
[24] T. Arima, Y. Tokura, J. B. Torrance, *Phys. Rev. B* **1993**, *48*, 17006.
[25] A. Chainani, M. Mathew, D. D. Sarma, *Phys. Rev. B* **1993**, *47*, 15397.
[26] S. Y. Smolin, A. K. Choquette, R. G. Wilks, N. Gauquelin, R. Felix, D. Gerlach, S. Ueda, A. L. Krick, J. Verbeeck, M. Bar, J. B. Baxter, S. J. May, *Adv. Mater. Interfaces* **2017**, *4*, 1700183.
[27] W. S. Choi, D. W. Jeong, S. Y. Jang, Z. Marton, S. S. A. Seo, H. N. Lee, Y. S. Lee, *J. Korean Phys. Soc.* **2011**, *58*, 569.
[28] a) J. Garcia-Barriocanal, F. Y. Bruno, A. Rivera-Calzada, Z. Sefrioui, N. M. Nemes, M. Garcia-Hernandez, J. Rubio-Zuazo, G. R. Castro, M. Varela, S. J. Pennycook, C. Leon, J. Santamaria, *Adv. Mater.* **2010**, *22*, 627; b) J. Garcia-Barriocanal, J. C. Cezar, F. Y. Bruno, P. Thakur, N. B. Brookes, C. Utfeld, A. Rivera-Calzada, S. R. Giblin, J. W. Taylor, J. A. Duffy, S. B. Dugdale, T. Nakamura, K. Kodama, C. Leon, S. Okamoto, J. Santamaria, *Nat. Commun.* **2010**, *1*, 1.
[29] Z. C. Zhong, P. Hansmann, *Phys. Rev. X* **2017**, *7*, 011023.
[30] A. J. Nelson, J. G. Reynolds, J. W. Roos, *J. Vac. Sci. Technol., A* **2000**, *18*, 1072.
[31] P. S. Bagus, R. Broer, W. A. de Jong, W. C. Nieuwpoort, F. Parmigiani, L. Sangaletti, *Phys. Rev. Lett.* **2000**, *84*, 2259.
[32] J. Topfer, A. Feltz, D. Graf, B. Hackl, L. Raupach, P. Weissbrodt, *Phys. Status Solidi A* **1992**, *134*, 405.
[33] F. M. F. Degroot, *J. Electron Spectrosc. Relat. Phenom.* **1994**, *67*, 529.
[34] B. Gilbert, B. H. Frazer, A. Belz, P. G. Conrad, K. H. Nealson, D. Haskel, J. C. Lang, G. Srajer, G. De Stasio, *J. Phys. Chem. A* **2003**, *107*, 2839.
[35] B. H. Frazer, B. Gilbert, B. R. Sonderegger, G. De Stasio, *Surf. Sci.* **2003**, *537*, 161.
[36] S. R. Spurgeon, Y. G. Du, S. A. Chambers, *Microsc. Microanal.* **2017**, *23*, 513.
[37] a) S. A. Chambers, Y. Liang, Y. Gao, *Phys. Rev. B* **2000**, *61*, 13223; b) T. C. Kaspar, T. C. Droubay, *J. Vac. Sci. Technol., A* **2012**, *30*, 04D112; c) E. A. Kraut, R. W. Grant, J. R. Waldrop, S. P. Kowalczyk, *Phys. Rev. Lett.* **1980**, *44*, 1620; d) E. A. Kraut, R. W. Grant, J. R. Waldrop, S. P. Kowalczyk, *Phys. Rev. B* **1983**, *28*, 1965.
[38] T. C. Kaspar, D. K. Schreiber, S. R. Spurgeon, M. E. McBriarty, G. M. Carroll, D. R. Gamelin, S. A. Chambers, *Adv. Mater.* **2016**, *28*, 1616.
[39] R. Comes, S. Chambers, *Phys. Rev. Lett.* **2016**, *117*, 226802.
[40] a) A. C. Tuan, T. C. Kaspar, T. Droubay, J. W. Rogers Jr., S. A. Chambers, *Appl. Phys. Lett.* **2003**, *83*, 3734; b) M. Cardona, *Phys. Rev.* **1965**, *140*, A651.
[41] M. W. Kim, P. Murugavel, S. Parashar, J. S. Lee, T. W. Noh, *New J. Phys.* **2004**, *6*, 156.
[42] N. C. Bristowe, P. B. Littlewood, E. Artacho, *Phys. Rev. B* **2011**, *83*, 205405.
[43] P. V. Sushko, K. M. Rosso, J. G. Zhang, J. Liu, M. L. Sushko, *Adv. Funct. Mater.* **2013**, *23*, 5530.
[44] a) G. Kresse, J. Furthmüller, *Phys. Rev. B* **1996**, *54*, 11169; b) G. Kresse, J. Hafner, *Phys. Rev. B* **1994**, *49*, 14251.
[45] P. E. Blöchl, *Phys. Rev. B* **1994**, *50*, 17953.
[46] J. P. Perdew, A. Ruzsinszky, G. I. Csonka, O. A. Vydrov, G. E. Scuseria, L. A. Constantin, X. L. Zhou, K. Burke, *Phys. Rev. Lett.* **2008**, *100*, 136406.
[47] S. L. Dudarev, G. A. Botton, S. Y. Savrasov, C. J. Humphreys, A. P. Sutton, *Phys. Rev. B* **1998**, *57*, 1505.
[48] a) R. Bader, *Atoms in Molecules: A Quantum Theory*, Oxford University Press, Oxford **1990**; b) W. Tang, E. Sanville, G. Henkelman, *J. Phys.: Condens. Matter* **2009**, *21*, 084204.